Physics of a strongly oscillating axisymmetric air-water interface with a fixed boundary condition

Cong Wang and Morteza Gharib

Phys. Rev. Fluids **7**, 044003 — Published 25 April 2022

DOI: 10.1103/PhysRevFluids.7.044003

Physics of a strongly oscillating axisymmetric air-water interface with a fixed boundary condition

Cong Wang* and Morteza Gharib

Division of Engineering and Applied Science,

California Institute of Technology, Pasadena, CA 91125, USA

(Dated: April 15, 2022)

Abstract

In this work, we experimentally investigate the physics of a strongly oscillating, millimeter-sized, axisymmetric air-water interface with a fixed contact line boundary condition. Many previous studies focused on the regime of small oscillation amplitude, e.g., $R = d/D \ll 1$, where d is the oscillation amplitude and D is the characteristic size of the air-water interface. The current investigation instead, focuses on a less studied oscillation regime with large R that is up to 0.33. The dynamic oscillations induce different steady streaming patterns, such as a low-speed streaming vortex or a fast-speed streaming jet. The steady streaming jet, in particular, was not much studied previously and is the major focus of this work. The streaming jet is only generated when the oscillating interface exhibits the higher-order axisymmetric oscillation modes with a large oscillation amplitude, which correspond to the regime with large R and large Weber number (We). The streaming jet has a larger Reynolds number ($Re \sim \mathcal{O}(100)$) than the typical streaming motions induced by an oscillating interface ($Re \sim \mathcal{O}(1)$). In addition, the streaming jet has a high ratio of the streaming velocity versus the oscillatory velocity, which suggests a high efficiency in generating steady streaming motion. The dynamic velocity and vorticity field of the streaming jet in both the initiation stage and the quasi-steady stage are presented, which demonstrate that the streaming jet onset process is a consequence of vorticity generation, transportation, and accumulation happening at the oscillating interface. As a zero-mass-flux jet, the streaming jet is sustained by entraining fluid mass flux from the circumferential regions, through a process similar to the classical Stokes drift. It is further found that a streaming jet can be induced by an oscillating elastic no-slip membrane as well, when the oscillation has large R and We. The extraordinary characters of the streaming jet can be employed in many engineering applications.

* cwwang@caltech.edu

I. INTRODUCTION

The dynamic oscillation of a free-slip air-water interface ubiquitously exists in both the natural world and many engineering systems, such as at the ocean surfaces. The periodic oscillations often generate non-trivial time-averaged mean velocity and vorticity, which is typically referred as steady streaming [1]. The phenomenon of steady streaming at a free surface can happen in different scenarios over a wide range of scales, which include but are not limited to Faraday waves [2], travelling surface waves [3], and cavitation bubble streaming [4 and 5], to name a few.

In particular, the steady streaming motion induced by the oscillation of a submerged cavitation bubble, which is typically referred as cavitation bubble streaming, has received paramount attention recently. Cavitation bubble streaming can be employed in a wide range of engineering applications. For example, the streaming motion induced by an oscillating micro-scale cavitation bubble is a powerful mechanism in microfluidics device systems for drug delivery [6], micro/bio-particle sorting, mixing and pumping [5 and 7]. The oscillation of a micro-bubble is typically driven by ultrasound waves within the frequency range of KHz to MHz and the induced streaming motions are low Reynolds number laminar flows. Generally speaking, fast-speed streaming motions with high Reynolds number is more effective in flow manipulation and therefore highly desired [8]. The cavitation bubble can be either free [4 and 9] or have the contact line of the air-water interface partially or fully attached to the solid surface [5 and 8]. The difference in the boundary condition substantially affects the oscillation modes of the interface and the streaming motions induced. The oscillation of a free bubble exhibits strong translation oscillation but weak volume oscillation, which generates low Reynolds number streaming motions ($Re \sim \mathcal{O}(0.1)$) [4]. In contrast, a partially or fully fixed oscillating bubble exhibits a strong volume oscillation and induces steady streaming motions with a faster speed and higher Reynolds number ($Re \sim \mathcal{O}(1)$) [1, 5, 8, and 9]. A typical streaming pattern induced by a fixed oscillating bubble is a fountain-shaped vortex system, where the streaming flow leaves from the center of the oscillating bubble and returns from the side regions [5]. The streaming fountain can be reversed to an anti-fountain shaped when the interface oscillates at a different oscillation mode with a higher frequency [5]. Rich theoretical analysis for the oscillation of both free bubble and fixed bubble has been done [8 and 9].

The oscillations of a free-slip interface and the associated streaming motions can be categorized based on a bunch of non-dimensional parameters as listed below. For an air bubble with a diameter D that oscillates at frequency f and amplitude d, a commonly used non-dimensional parameter is the non-dimensional oscillation amplitude $R = \frac{d}{D}$. The oscillation induces a characteristic oscillatory velocity $u_o = fd$ in the surrounding regions because of continuity. In this regard, the Weber number defined as $We = \frac{\rho(u_o)^2 D}{\gamma}$ (ρ is the density of water, and γ is the surface tension effect), is used to quantify the relative significance of the unsteady inertia force versus the surface tension effect. In the current scenario, the Weber number is effectively $We = \frac{\rho(fd)^2 D}{\gamma}$. Furthermore, an unsteady Reynolds number based on the oscillatory velocity u_o can be defined as $Re = \frac{fdD}{\nu}$ (ν is the kinetic viscosity) and a streaming Reynolds number based on the maximum streaming velocity u_s can be defined as $Re_s = \frac{u_s D}{\nu}$. In most of the previous cavitation bubble streaming studies, the oscillations were in the regime with small R, We and Re, i.e., $R \ll 0.05$ and $Re \sim \mathcal{O}(\infty)$ [4, 5, and 8]. The small R is also a fundamental requirement in many theoretical and analytical studies [1 and 9].

In this work, we investigate the dynamic oscillations of a millimeter sized, axisymmetric air-water interface with a fixed contact line boundary condition. The experimental apparatus is schematically shown in figure 1. First, a circular shaped surface cavity is created over a flat surface as an air-pocket. The inner surface of the cavity is selectively coated with supper-hydrophobic materials whereas the flat outer surface of the cavity is coated with super-hydrophilic material. As such, sharp wettability change is created at the edge of the surface cavity. The sharp wettability change ensures that the contact line of the air-water interface is fixed at the edge of the surface cavity when the flat surface is immersed into water. The oscillation of the free-slip interface is driven by modulating the dynamic pressure inside the surface air-pocket through the usage of a dynamic pressure source (e.g. a speaker) and a sealed air-chamber. In addition, the static curvature of the interface can be accurately adjusted by controlling the static air pressure inside the surface cavity. The interface is set to face downward so that the upward buoyancy force stabilizes the oscillating interface. The experimental design enables large amplitude dynamic oscillations (i.e., large R) without the disintegration of the air-water interface. The strong oscillations induce interesting steady streaming motion patterns. Among the different streaming patterns, the most extraordinary case is a fast-speed, far-propagating streaming jet. The dynamic features of the streaming

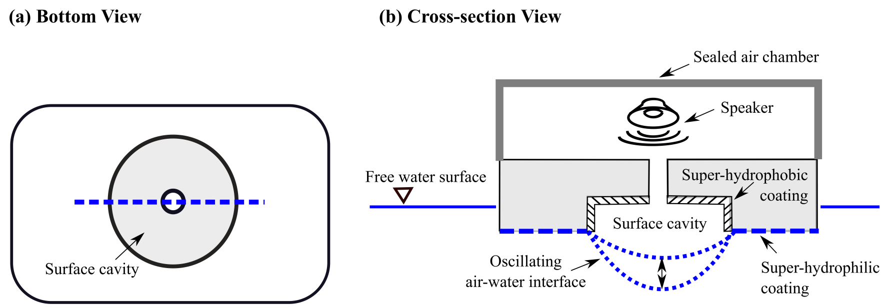

FIG. 1. Schematic drawing of an oscillating free-slip air-water interface with a fixed contact line boundary condition. The contact line of the air-water interface is fixed at the edge of a surface cavity by applying super-hydrophobic and super-hydrophilic material coating in different regions of the surface cavity. The static and dynamic curvature of the interface is controlled by regulating the static and dynamic pressure inside the surface cavity. The dashed line in panel (b) marks the location of the experiment measurement plane.

jet and the physical mechanism to generate the streaming jet are the major focuses of this paper.

The rest of this paper is organized as follows. In Section II, the detailed experimental setup and information of the test cases are given. The dynamic oscillations and the associated streaming motions are presented and analyzed in Section III. Section IV is devoted to demonstrating the special case of a fast-speed streaming jet. Section V presents the results of an oscillating no-slip elastic surface. Section VI discusses the presented results and Section VII concludes this work.

II. EXPERIMENTAL SETUP

The experimental setup is schematically shown in figure 2. The experiment was conducted in a 50 cm long, 25 cm wide, and 25 cm deep water tank with transparent walls. The surface air-pocket had a diameter $D = 8mm$ and was located at the center of a 75 mm by 150 mm flat surface. The flat surface was immersed 10 mm beneath the free water surface to ensure that the oscillating interface is far away from the free surface and the wall of the water tank. The static curvature of the interface was maintained to be either flat or 1.5 mm bulged-out of the surface cavity into the water below. The corresponding radius of curvature of the interface (κ) was ∞ and 6.1 mm, respectively.

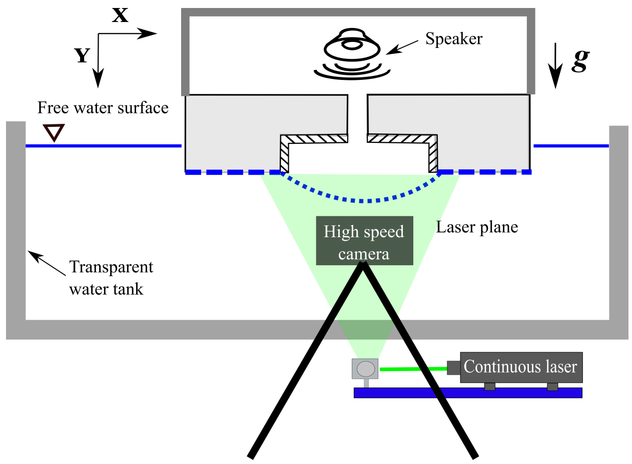

FIG. 2. Schematic experimental setup where a high-speed camera and a continuous laser were employed to conduct high resolution digital particle image velocimetry (DPIV) in the central plane of the axisymmetric air-water interface (marked by the dashed line in figure 1 (b)). The Cartesian coordinate system and the gravitational direction are also shown.

The input voltage of the dynamic pressure source was kept constant, and the modulation frequency was varied within the range from 5 Hz to 100 Hz. With this setting, the modulation power input for all the test cases are the same. The diaphragm of the speaker oscillated with the same amplitude, which was confirmed by high speed video recordings of the oscillating diaphragm. As such, the dynamic modulation pressure of the air-water interface has constant oscillation amplitude. When the dynamic pressure modulation has large amplitude and high frequency, irregular capillary waves can be excited at the oscillating interface. In this study, the input voltage signal was adjusted such that the interface only oscillates axisymmetrically for all the selected frequencies. The axisymmetry of the dynamic oscillation was confirmed by the video recording of the oscillating interface using a high-speed camera.

In addition to the dynamic oscillation of a free-slip interface, the dynamic oscillation of a no-slip elastic membrane was also investigated. The elastic membrane is 30 μm thick and can be stretched up to 400% of its original size. The material of the membrane and the fabrication procedure are given in Appendix A. The surface tension of the elastic membrane is 30 N/m, approximately 416 times larger than that of the surface tension of an air-water interface. The no-slip elastic membrane was kept the same size and oscillated within the same frequency range as the free-slip interface.

We conducted high fidelity digital particle image velocimetry (DPIV) to quantitatively map the dynamic velocity and vorticity field of the oscillatory motion and the steady streaming motion. The water phase was seeded with neutrally buoyant particles with a 13 μm diameter (manufactured by *Potters Industry*) and was illuminated by a continuous laser plane that cuts through the center of the interface. A high-speed camera (*TSI* Y7 model) was used to record the dynamic particle movements near the oscillating interface at a high frame rate. The frame rate was adjusted such that for all the tested frequencies, images at 20 equally spaced phases are recorded per oscillation cycle.Based on the acquired image sequences, velocity and vorticity field with a high spatial and temporal resolution can be obtained. The dynamic features of the periodic velocity and vorticity field can be extracted by phase-averaging the velocity and vorticity field. In addition to DPIV measurements, the profiles of the oscillating interface are tracked. The qualitative flow pathline visualization was also adapted to demonstrate the dynamic oscillation and the steady streaming motion.

III. DYNAMIC OSCILLATION AND THE INDUCED STEADY STREAMING MOTION

In this section, the different dynamic oscillations and the associated steady streaming motions are presented and analyzed.

A. Dynamic oscillations

Figure 3 shows the snapshots of the oscillating interfaces at 20 Hz, 30 Hz, or 50 Hz, with either a flat or bulged-out static configuration. The snapshots are at 5 equally spaced phases (ϕ) over the period of one oscillation cycle (T). The high resolution video recording of the oscillating interface is shown in the Supplementary Video 1. Depending on the oscillation frequency and the static curvature of the interface, the interfaces exhibited different oscillation modes with varied oscillation amplitude, although the dynamic pressure had a constant modulation amplitude for all the test cases. Generally speaking, when the interface had a flat configuration and oscillated at low frequencies (i.e., the cases shown in panel (a) and (b)), the curvature of the interface was approximately uniform at each phases and the oscillation amplitude was relatively small. In contrast, when the interface had a bulged-out configuration or oscillated at the higher frequencies (i.e., the cases shown in panel (c), (e)

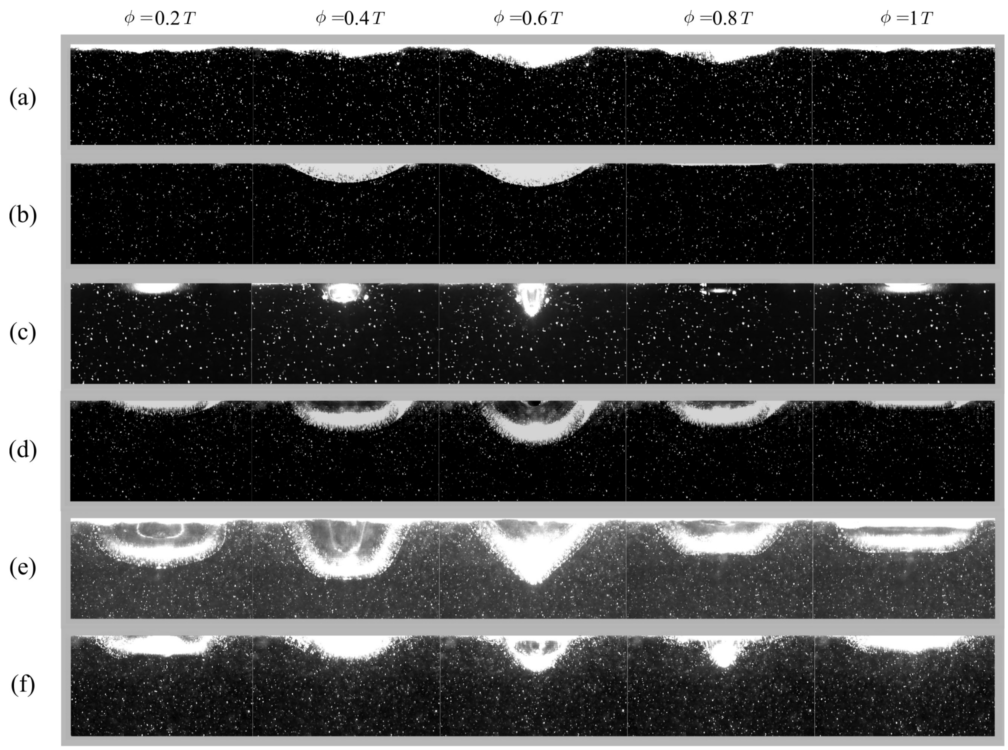

FIG. 3. Snapshots of the dynamic free-slip surface at 5 equally spaced phases (ϕ) over the period of one oscillation cycle (T). The static interface was either flat (panel (a), (b), (c)) or bulged-out (panel (d), (e), (f)). The modulation frequency was 20 Hz (panel (a), (d)), 30 Hz (panel (b), (e)), and 50 Hz (panel (c), (f)).

and (f)), the interface exhibited sharp local curvatures at certain phases and had a relatively large oscillation amplitude.

Among all the test cases shown in figure 3, the oscillation amplitude d peaks when the interface has bulged-out configuration and oscillates at 30 Hz (panel (d)), which could be due to several reasons. First, the oscillating interface as a consequence of air bubble volume expansion and contraction, can be affected by its static volume. Assuming the interface has a static volume V_s and an oscillating volume $V_0 sin(2\pi ft)$, the oscillation amplitude d is of the order $\mathcal{O}(\sqrt[3]{V_s + V_0 sin(2\pi ft)} - \sqrt[3]{V_s})$. As such, if V_s is initially large (e.g., the interface is bulged-out), the oscillation amplitude d will be small. Second, the oscillation is affected by the surface tension effect, which depends on the static curvature of interface. Due to the contribution of the two factors, an optimal static curvature in the middle ground could exist. The frequency dependence of d arises from the impedance of the system, mainly due to the added mass effect and the viscous stress of the unsteady motions in water [10]. The contribution from air is negligible due to the much smaller density and viscosity of air. When the oscillation frequency is high, the large impedance of the system suppresses the oscillation amplitude. In addition, the intrinsic oscillation amplitudes of the different oscillation modes are different, which also contribute to the difference in the effective oscillation amplitude d. These factors could have contributed to the sweet spot for creating large amplitude oscillations in the parameter space of the static curvature and the oscillation frequency.

The profiles of the bulged-out interfaces oscillating at 20 Hz, 30 Hz and 50 Hz are shown in figure 4 (a) - (c), respectively. The profiles resemble the first and second axial-symmetric oscillation modes of the Bessel function J_{01} and J_{02}, or the combination of both modes. The basic mode J_{01} is preferentially excited by the low-frequency oscillations whereas the higher-order J_{02} mode is preferentially excited by the high-frequency oscillations. Indeed, it was theoretically shown that the oscillation of an axisymmetric elastic surface in a viscous fluid with a fixed boundary condition is a modified Bessel function [11]. The axisymmetric profiles in figure 4 indicate that the oscillating interfaces are essentially axisymmetric standing waves. The wavelength of the standing waves are upper limited by the 8 mm diameter of the surface cavity, with the higher-order oscillation modes having a shorter wavelength. The critical wavelength to distinguish gravity wave and capillary wave is 17 mm, and the regime with a shorter wavelength is dominated by the surface tension effect and referred as the capillary regime. As such, the current oscillating interfaces are capillary waves. As shown by the case in figure 4 (c), the capillary waves has a very steep wave slope when the higher-order oscillation modes are excited. The steep capillary wave as a highly nonlinear and sometimes even singular phenomenon, has been investigated in different scenarios both experimentally and theoretically [12–15].

B. Steady streaming motions

The dynamic oscillations induce steady streaming motions with different patterns, as qualitatively shown by the flow pathlines (within the period of 1 second time) in figure 5 (a) - (f). The dark to bright color change of the flow pathlines demonstrates the direction of time. With a flat interface oscillating at low frequencies (panel (a) and (b)), a small ring-shaped vortex is generated near the oscillating interface; With a bulged-out interface oscillating at higher frequencies, (panel (c), (e), and (f)), a streaming jet that can propagate

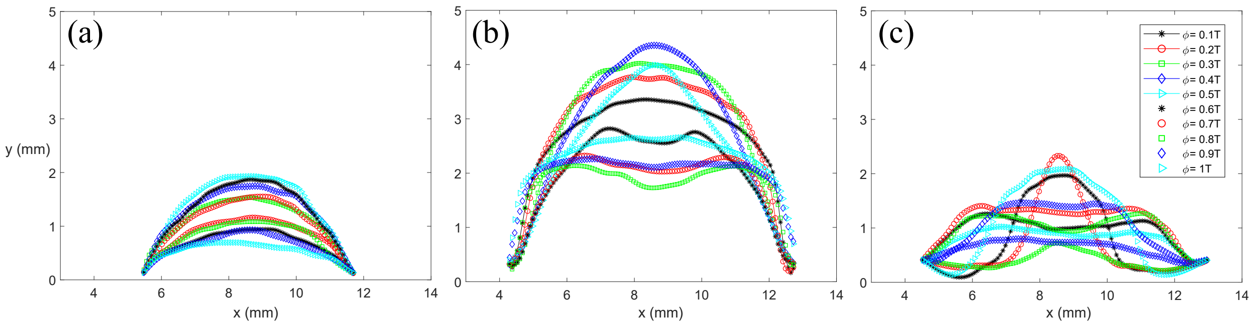

FIG. 4. The phase-varying profiles of a bulged-out interface oscillating at (a) 20 Hz, (b) 30 Hz and (c) 50 Hz. The dynamic oscillations resemble the different modes of the Bessel function. The oscillation amplitude peaks at 30 Hz among the selected frequencies.

far away along the central axis is generated. In the middle ground regime, i.e., case (d), an elongated streaming vortex is created.

The time-averaged velocity contour for the three bulged-out oscillating interfaces are shown in figure 6, where the 30 Hz oscillation case has the fastest streaming velocity u_s. The steady streamlines as shown by the grey arrow curves demonstrate the different streaming patterns. The stream jet as a zero-mass-flux jet is sustained by entraining mass flux from the circumferential region of the oscillating interface. The steady streamlines also demonstrate the entrainment process in the circumferential regions, which will be further presented in details in section IV.

C. Non-dimensional parameters

Table I lists out the values of the non-dimensional parameters associated with the dynamic oscillations and the steady streaming motions, based on the definitions given in Section I. As shown by the profiles of interface in figure 4,the oscillation amplitude d has different values depending on the measurement location. Here the largest d at the center of the oscillating interface is used to evaluate the relevant non-dimensional parameters. As shown in table I, the non-dimensional oscillation amplitude R is within the range of $0.14 - 0.33$, and the Weber number We varies from 0.05 to 0.8. The Reynolds number based on the oscillatory velocity Re is within the range of $180 - 670$ and the streaming Reynolds number Re_s is within the range of $5 - 360$. Furthermore, the ratio of the streaming Reynolds number versus the oscillatory Reynolds number $\frac{Re_s}{Re}$, which is equivalent to the ratio of the streaming

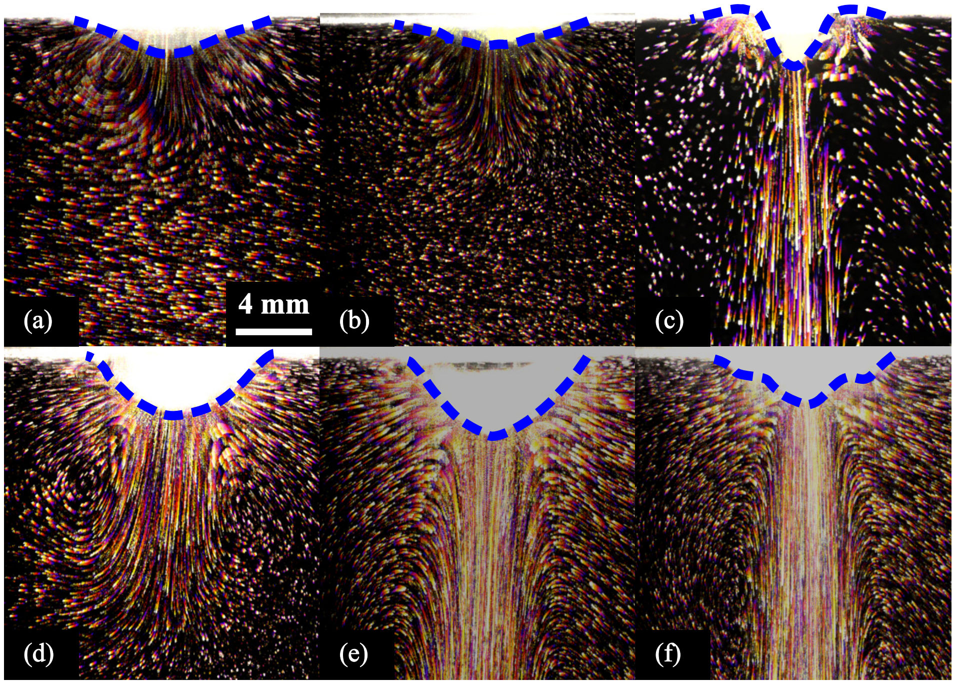

FIG. 5. Flow pathlines (in 1 second time) showing the steady streaming motions induced by the different dynamic oscillations, with the same panel labeling as figure 3. The out-most boundary of the oscillating interface is highlighted by the blue dashed lines. The observed streaming patterns include small-scale streaming vortex and large-scale streaming jet as well as a transitional streaming vortex in between.

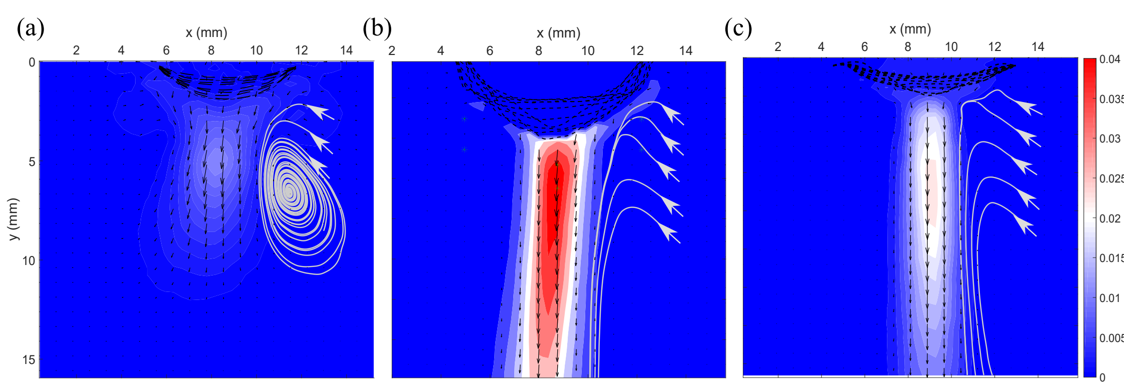

FIG. 6. Mean velocity contour associated with an oscillating bulged-out interface (a) 20 Hz, (b) 30 Hz, and (c) 50 Hz. The 30 Hz case has the fastest streaming velocity. The streamlines (grey arrow curves) demonstrate the different streaming patterns and entrainment processes.

Case	R	We	Re	Re_s	$\frac{Re_s}{Re}$
Flat interface, 20 Hz (vortex)	0.14	0.05	179	5	0.03
Flat interface, 30 Hz (vortex)	0.23	0.32	441	17	0.04
Flat interface, 50 Hz (jet)	0.20	0.71	640	94	0.15
Bulged-out interface, 20 Hz (elongated vortex)	0.16	0.08	205	86	0.42
Bulged-out interface, 30 Hz (jet)	0.33	0.68	634	358	0.57
Bulged-out interface, 50 Hz (jet)	0.21	0.80	672	184	0.27

TABLE I. Values of the non-dimensional parameters for all the test cases.

velocity over the oscillatory velocity $\frac{u_s}{u_o}$, is also shown. A higher $\frac{Re_s}{Re}$ ratio indicates a higher efficacy in creating steady streaming motion by dynamic oscillations.

In many of the previous cavitation bubble streaming studies, the dynamic oscillation and steady streaming are in the regime of $R \leq 0.05$, $We \ll 1$, and $Re \sim \mathcal{O}(1)$ [4, 5, and 8]. The parameter values in table I suggest that the streaming vortex and the streaming jet are created by oscillations with much larger R. When compared to the streaming vortex, the streaming jet is created by oscillations with larger R and We. A streaming pattern phase diagram based on R and We is shown in figure 7. The approximated boundary of the streaming pattern change is shown by the grey dashed line. The phase diagram is far from complete because of the limited parameter range and data points. In addition to the streaming vortex and the streaming jet, many other streaming motion patterns can be generated by the dynamic oscillations in other regimes. Future investigations are needed to complete the phase diagram, which is beyond the scope of the current investigation.

The streaming jet has a $Re_s \sim \mathcal{O}(100)$ whereas the streaming vortex has a $Re_s \sim \mathcal{O}(10)$. As such, the streaming jet has a much faster streaming speed than the streaming vortex. In addition, the Reynolds number ratio $\frac{Re_s}{Re}$ of the streaming jet is an *order-of-magnitude* larger than that of the streaming vortex, which suggests the streaming jet has a higher efficient in creating steady streaming motion. The extraordinary characters of the streaming jet and the potential applications will be further discussed in Section VI.

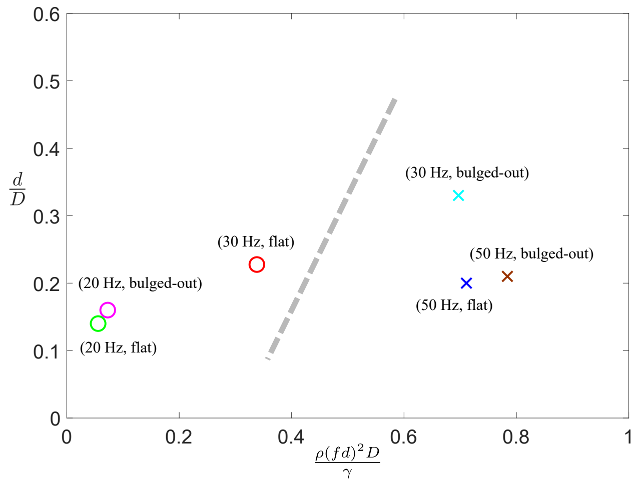

FIG. 7. Phase diagram of the different streaming patterns based on the non-dimensional amplitude ($R = \frac{d}{D}$) and the Weber number ($We = \frac{\rho(fd)^2 D}{\gamma}$). Circle: streaming vortex; Cross: streaming jet. Grey dashed line: an approximate boundary of streaming pattern change.

IV. PHYSICS OF THE STEADY STREAMING JET

In this section, the dynamic velocity and vorticity field of the steady streaming jet are presented and analyzed. For demonstration purpose, the case with a bulged-out interface oscillating at 30 Hz is selectively analyzed. Results of the streaming jet in both the initiation stage and the quasi-steady stage are shown.

A. Streaming jet in the initiation stage

To demonstrate the onset of the streaming jet, the interface was oscillated from its static state. The qualitative particle movement is synchronized with the time-varying velocity vector (u, v) and transverse vorticity ($\omega_z = \frac{\partial v}{\partial x} - \frac{\partial u}{\partial y}$) in the first 20 oscillation cycles. The complete streaming jet onset process is given in the Supplementary Video 2, with the key snapshots at the 1^{st}, 5^{th}, and 10^{th} oscillation cycle shown in figure 8. The boundary profile of the oscillating interface is also shown. Because of the axisymmetry of the dynamic oscillation, ω_z reflects the ring-shaped vorticity in the three-dimensional space. The streaming jet onset can be approximately divided into two stages. The first stage corresponds to the first 5 oscillation cycles, during which ω_z with alternative signs was periodically generated at the oscillating interface and transported to the central region of the interface. During this stage, the oscillation mode of the interface gradually evolves from the basic oscillation mode to a higher-order oscillation mode. As shown in panel (b), at the end of the 5^{th} oscillation cycle, a sharp central curvature of the interface appears. However, there is no streaming jet or a time-averaged vorticity $\overline{\omega_z}$ created during this stage. After the first 5 oscillation cycles, the dynamic oscillation reached a quasi-steady state in which a time-averaged vorticity $\overline{\omega_z}$ is continuously transported to the central region cycle by cycle. The ring-shaped vorticity accumulates along the symmetry axis, which leads to the formation of the streaming jet (shown in panel (c)).

To quantitatively demonstrate the streaming jet onset, the time series of the vertical velocity ($V(t)$) and the transverse vorticity ($\omega_z(t)$) measured at the (x, y) location of (7.7 mm, 10 mm) are shown in figure 9. The measurement location is in the pathway of the streaming jet but sufficiently far away from the oscillating interface. As such, the time series will reflect the temporal evolution of the flow structure of the streaming jet. The time-averaged velocity $\overline{V(t)}$ over the period of two oscillation cycles is also presented. As shown in figure 9, in the first 6 oscillation cycles, $V(t)$ periodically oscillates with a zero-mean value, which suggests no streaming jet is created. During the same period of time, ω_z is zero. After the first 6 oscillation cycles, $\omega_z(t)$ and $\overline{V}$ increases simultaneously indicating the arrival of the streaming jet. Both $\omega_z(t)$ and $V(t)$ reaches the plateau state after another 3 - 4 oscillation cycles, when the streaming jet reaches the quasi-steady stage. From the perspective of vorticity dynamics, the accumulated vorticity $\overline{\omega_z}$ induces the time-averaged velocity $\overline{V}$ to create the streaming jet, following the Biot-Savart law [16]. As such, the streaming jet is a consequence of vorticity generation, transportation, and accumulation process at the oscillating free-slip oscillating interface.

The fundamental mechanisms of vorticity generation and transportation at a free-slip interface have been studied in many different scenarios, both theoretically and experimentally. As an example, the seminal analysis in [17] demonstrates that a curved free-slip interface is a source of vorticity. When the curvature of the interface dynamically changes, a time-averaged vorticity and velocity field is created. In addition, [18] demonstrated that the dynamic curvature of a free-slip interface effectively manipulates the transportation flux of vorticity into the bulk fluid regime. The streaming jet onset process presented in the above exhibits features of these fundamental principles. However, to uncover the detailed physics of the streaming jet onset requires future in-depth investigations.

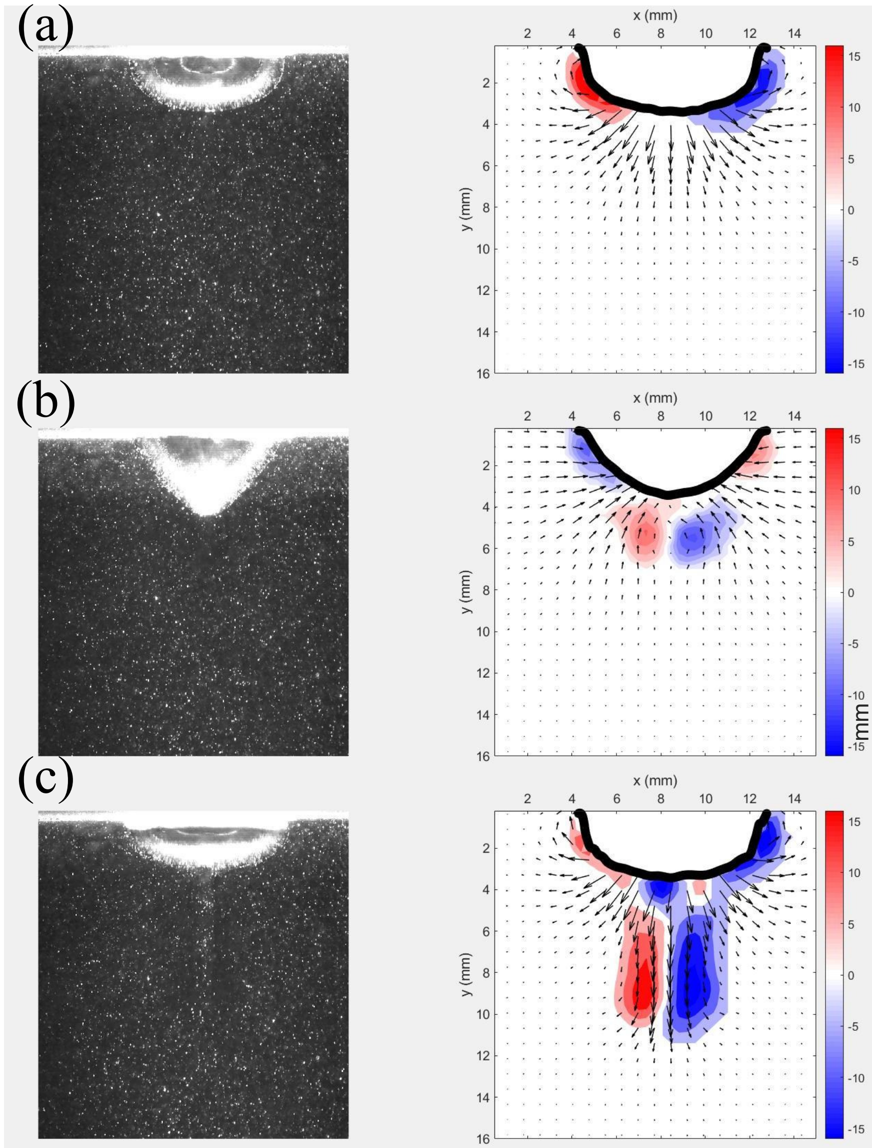

FIG. 8. Snapshots of the synchronized particle movement and velocity and vorticity contour in the initiation process of the streaming jet. The three snapshots are in (a) the 1^{st} oscillation cycle (b) the 5^{th} oscillation cycle and (c) the 10^{th} oscillation cycle. The accumulation of the ring-shaped vorticity along the symmetric axis corresponds to the formation of the jet.

B. Streaming jet in the quasi-steady stage

The streaming jet in the quasi-steady state is shown by the contours of the phase-averaged velocity in figure 10 and in the Supplementary Video 3. The contour color reflects the velocity magnitude and the vector arrows shows the velocity direction. Figure 10 suggest that the streaming jet happens together with a strong oscillatory motion in the near-field of the

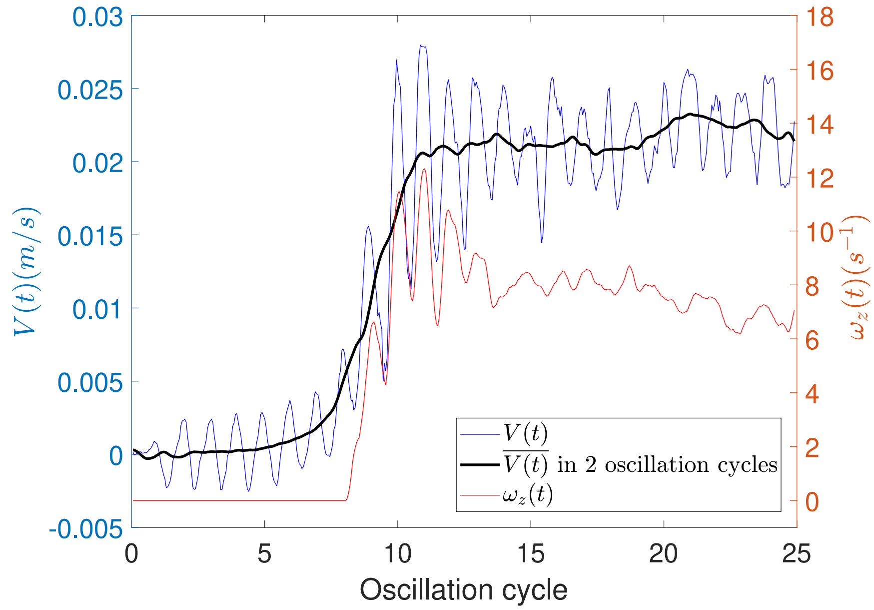

FIG. 9. Synchronized time series of the vertical velocity ($V(t)$) and the transverse vorticity ($\omega_z(t)$) measured at the (x, y) location of (7.7 mm, 10 mm), which is along the symmetry axis and far away from the oscillating interface. The streaming jet is created and sustained because the accumulated $\overline{\omega_z}$ induces a steady vertical velocity following the Biot-Savart law.

oscillating interface. The spatial transition of the near-field oscillatory motion to the steady current in the far-field is depicted by the phase-averaged vertical velocity $\widetilde{v}$ measured at 5 mm, 13 mm, and 20 mm away from the solid surface, which are shown in figure 11 (a) (c), respectively. In panel (a), the velocity profiles are strongly phase-dependent and exhibits features of a steep travelling wave from the edge region of the interface toward the center. In panel (c), the far-field velocity profiles are almost identical and phase independent. In panel (b), the velocity profiles exhibits combined features of dynamic oscillation and steady streaming.

The streaming jet is sustained by entraining mass flux in the circumferential region, as was shown by the steady streamlines in figure 6. The dynamic entrainment process can be qualitatively visualized by the flow pathlines over the period of one oscillation cycle, as is given in panel (L) of figure 12. In the region where the streaming jet exists, the flow pathlines are vertical straight lines; in the circumferential entrainment regions, the flow pathlines are closed-loop circles. These circles are the footprints of transverse travelling waves at the interface, which continuously transports water molecules toward the center of

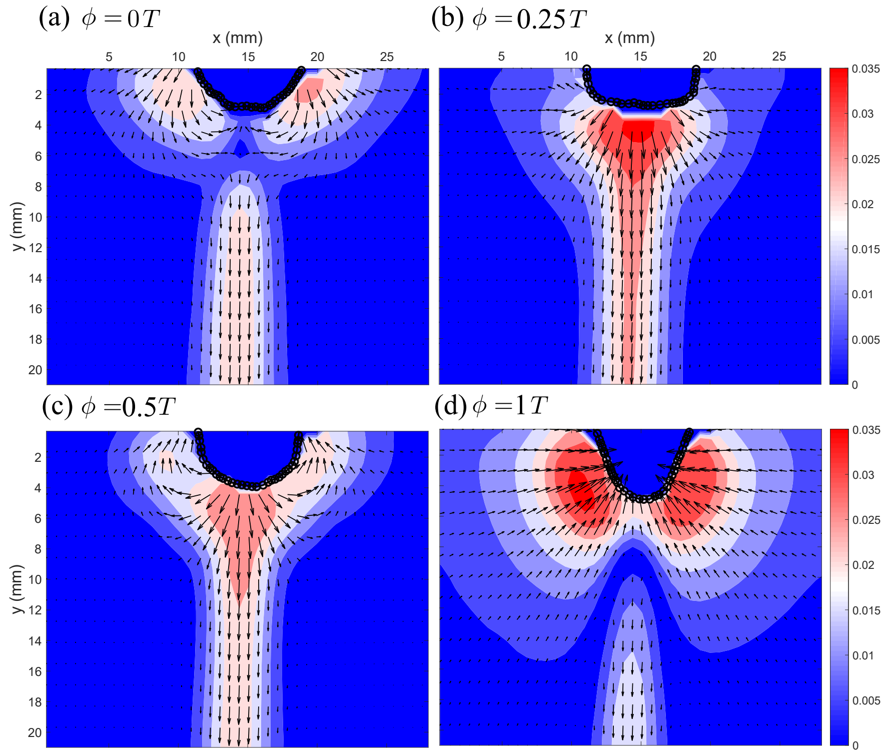

FIG. 10. Phase-averaged velocity vector contour at 4 equally spaced sample phases. The contour color shows the velocity magnitude (unit: m/s) and the vector arrows shows the velocity direction.

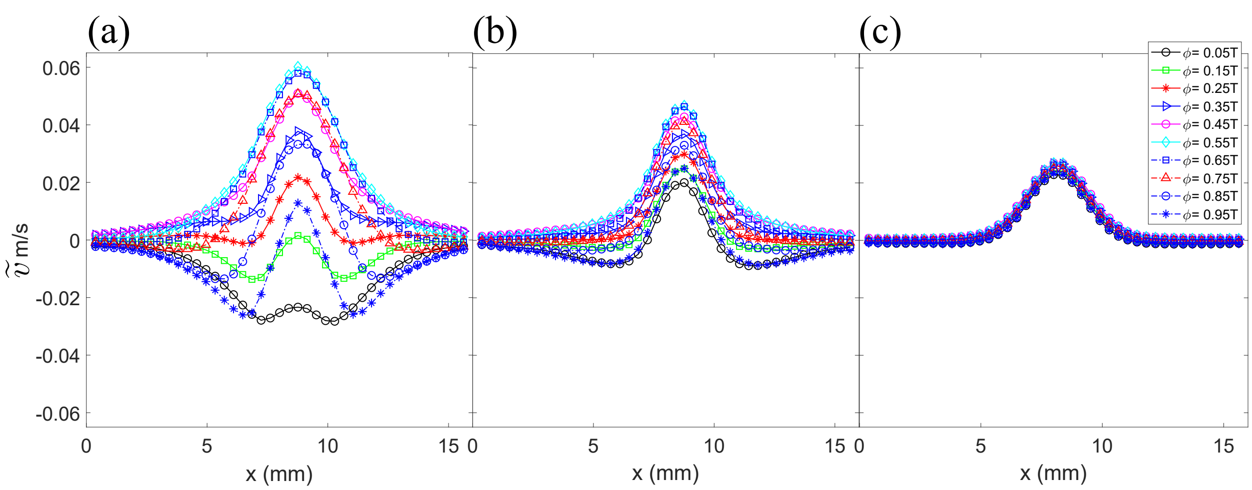

FIG. 11. Phase-averaged vertical velocity $\widetilde{v}$ measured at (a) y = 5 mm, (b) y = 13 mm, and (c) y = 20 mm. The near-field velocity exhibits features of a steep traveling wave whereas the far-field velocity reflects a steady current.

the interface. Figure 12 panel (R) demonstrates the phase-plane plots of the phase-averaged velocity vector $(\widetilde{u}, \widetilde{v})$ at locations labeled as (a) (e) in panel (L). Location (a) (d) are in the circumferential entrainment regions whereas location (e) is in the jetting region. In the circumferential entrainment regions, $(\widetilde{u}, \widetilde{v})$ are in elliptical shapes. The orientation and the effective radius of the $(\widetilde{u}, \widetilde{v})$ ellipse reflects the direction of the travelling wave and the magnitude of the velocity vector. In contrast, the $(\widetilde{u}, \widetilde{v})$ in panel (e) has a v component but not u component. As such, the oscillation in this region behaves like a longitudinal wave rather than a transverse wave. In addition to $(\widetilde{u}, \widetilde{v})$, the mean velocity vector $(\overline{u}, \overline{v})$ is shown by the red dots in each panel, which is visualized by the black arrows. The dashed arrows in panel (a) (d) is amplified 10 times to demonstrate the small mean velocity vector whereas the solid arrow in panel (e) is not amplified. As such, the mean velocity of the jet is at least an order-of-magnitude larger than that of the entrainment. For the entrainment regions shown in panel (a) (d)), the magnitude of the mean velocity is quadratic of the magnitude of the oscillatory velocity, i.e., $|(\overline{u}, \overline{v})| \sim \mathcal{O}(|(\widetilde{u}, \widetilde{v})|^2)$, which is similar to the classical Stokes drift and many other streaming phenomena at a free surface [17, 19, and 20].

V. OSCILLATION OF A NO-SLIP ELASTIC MEMBRANE

The oscillating free-slip interface has a coupled dynamic oscillation effect and a free-slip effect, both of which could have contributed to the generation of the streaming jet. As such, a natural question is, which effect is the dominant factor? To decouple the oscillation effect from the free-slip effect, an 8 mm sized, highly-stretchable *no-slip* elastic membrane was forced to oscillate at 50 Hz by the same actuation mechanism. As was mentioned in Section II, the elastic membrane has surface tension effect more than 400 times larger than the same sized air-water interface. To overcome the much stronger surface tension effect, the input power of the modulation signal was increased to be 2 times or 30 times large of the original modulation power setting. These two modulation power settings will be referred as low-power modulation and high-power modulation in what follows. The elastic membrane was statically flat and the oscillation in and out of the surface cavity was approximately symmetric with respect to the flat neutral position. Unlike the cases with a 50 Hz oscillating free-slip interface, the elastic membrane only exhibited the basic oscillation mode when actuated by both the low-power and high-power modulation. The absence of the

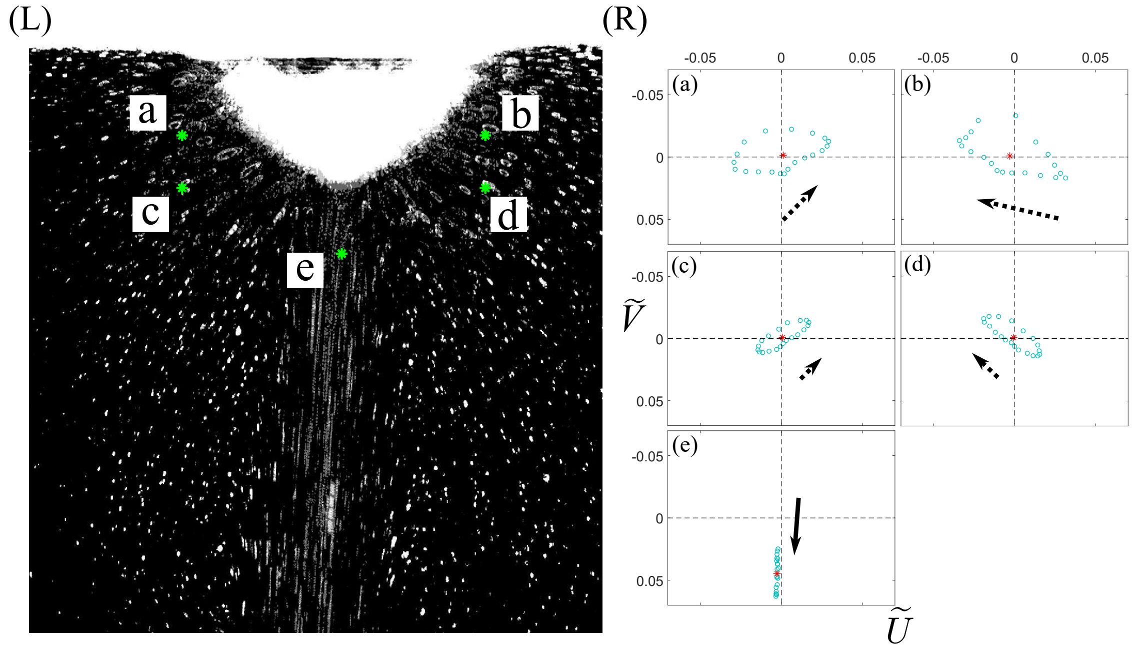

FIG. 12. Panel (L): Flow pathlines near a 30 Hz oscillating bulged-out interface over the period one oscillation cycle. In the circumferential entrainment regions (e.g., labeled as (a) - (d)), the flow pathlines are closed-loop circles. In the jetting region, the flow pathlines are vertical straight lines. Panel (R): Phase-plane plots for the phase-averaged velocity vector $(\widetilde{u}, \widetilde{v})$ at locations labeled as (a) (e) in panel (L). Blue circles: $(\widetilde{u}, \widetilde{v})$; Red dots: $(\overline{u}, \overline{v})$; Arrows: visual representation of the time-averaged velocity vector $(\overline{u}, \overline{v})$. The dashed arrows in panel (a) (d) are amplified 10 times whereas the solid arrow in panel (e) is not amplified.

higher-order oscillation modes is likely due to the suppression effect of the much stronger surface tension of the elastic membrane. The low-power modulation induced a fountain-shaped streaming pattern whereas the high-power modulation induced a streaming jet, as qualitatively shown by the flow pathlines over the period of 3 oscillation cycles in figure 13 (a) and (b), respectively. The streaming jet is more clearly shown by the video recording in the Supplementary Video 4.

The values of the non-dimensional parameters for both the low-power and the high-power modulation cases are shown in Table II. Similar to the oscillating free-slip interface, the steady streaming jet is preferentially induced by the oscillation with larger R and larger We. However, the Reynolds number ratio $\frac{Re_s}{Re}$ of the streaming jet here is lower than those induced by an oscillating free-slip interface shown in Table I.

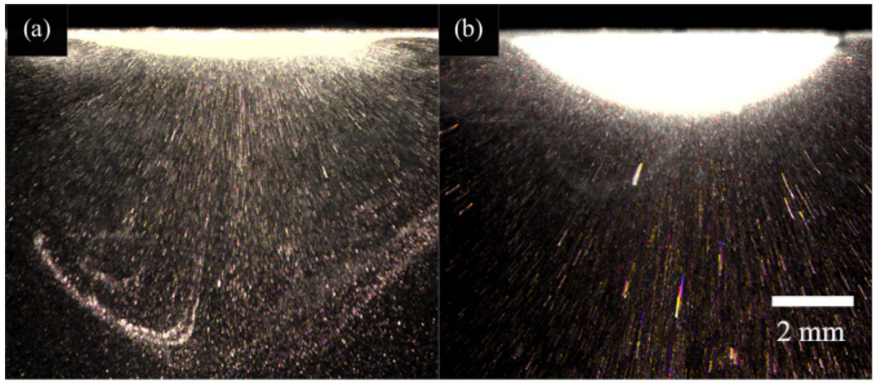

FIG. 13. Flow pathlines over the period of 3 oscillation cycles for a 50 Hz oscillating no-slip elastic membrane under (a) low-power modulation and (b) high-power modulation.

Case	R	We	Re	Re_s	$\frac{Re_s}{Re}$
Low-power modulation	0.14	0.008	450	11	0.023
High-power modulation	0.46	0.010	1470	201	0.140

TABLE II. Non-dimensional parameters for a 50 Hz oscillating no-slip elastic membrane when actuated by low-power modulation and high-power modulation.

The mean velocity contour for the two different power modulation cases are shown in figure 14 (a) and (b), with the steady streamlines and the profile of the most bulged-out elastic membrane also shown. The streaming velocity u_s in panel (a) is about 10 times slower than that in panel (b). For the streaming jet case, the profiles of the phase-averaged velocity $\widetilde{v}$ at $y = 5$ mm and $y = 13$ mm are shown in figure 15 (a) and (b), respectively. At $y = 5$ mm, $\widetilde{v}$ is approximately symmetric in the positive and negative y direction. As such, the time-averaged $\overline{v}$ is small. At $y = 13$ mm, $\widetilde{v}$ is generally positive at the central region, indicating the existence of a steady streaming jet. In addition to the steady jet, a strong oscillatory $\widetilde{v}$ also exists. In the regions out of the streaming jet, $\widetilde{v}$ averages to zero. This observation implies the oscillating membrane has a low efficacy in creating steady streaming motion, which is consistent with the low $\frac{Re_s}{Re}$ ratio in Table II. The very different $\frac{Re_s}{Re}$ in Table I and Table II seems due to the different oscillation modes: a higher-order oscillation mode is more efficient in creating steady streaming motion. Both a free-slip air-water interface and a no-slip elastic membrane can produce a streaming jet when oscillation is in certain regimes. As such, we conclude that the streaming jet generation is mainly due

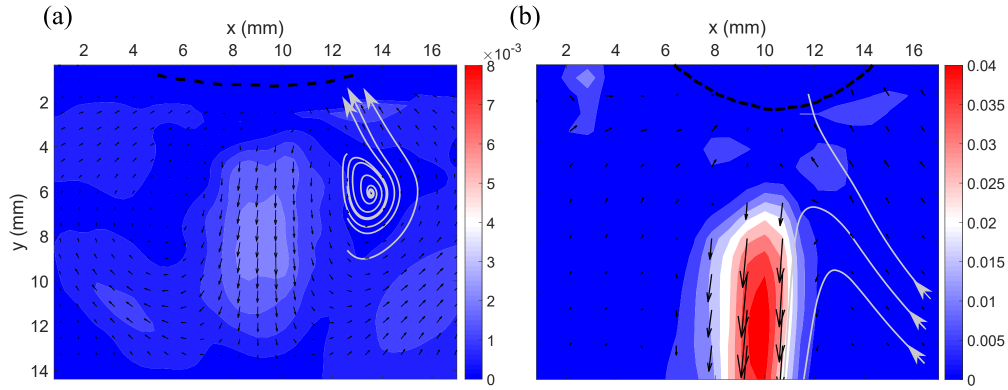

FIG. 14. Time-averaged velocity contour for the 50 Hz oscillating no-slip elastic membrane under (a) low-power modulation and (b) high-power modulation. Note the contour scales are different in the two panels.

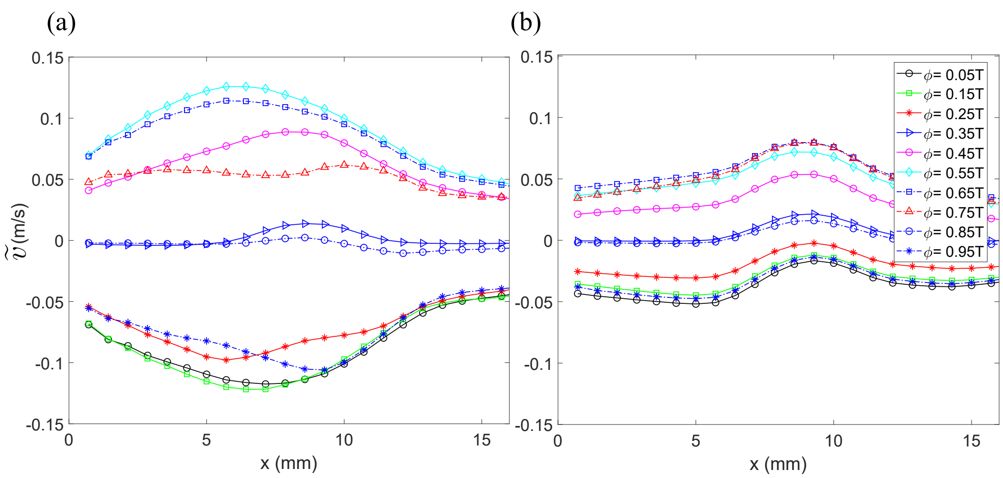

FIG. 15. Phase-averaged vertical velocity $\widetilde{v}$ measured at (a) y= 5 mm and (b) y = 13 mm for the streaming jet created by the high power modulation. In panel (a), $\widetilde{v}$ is approximately symmetric. In panel (b), features of steady streaming jet is observed. In addition, $\widetilde{v}$ also exhibits features of strong oscillatory motion in regions both within and out of the streaming jet.

to the dynamic oscillation effect rather than the free-slip effect.

VI. DISCUSSION

The steady streaming jet created by the dynamic oscillation of a free-slip air-water interface is a fundamental phenomenon that should happen at all length scales, as long as the non-dimensional parameters are in the right regime. The presented results suggest that the creation of the streaming jet is linked to the excitation of the higher-order axisymmetric oscillation modes with a large oscillation amplitude at the free-slip interface. It was found that the higher-order oscillation modes can be excited over a micro-bubble by KHz oscillations [21]. As such, we expect the generation of a micro-scale streaming jet by an oscillating micro-bubble. The oscillation should have higher frequencies but smaller amplitudes. The extraordinary characters of the streaming jet, such as the high efficacy in generating fast-speed steady streaming motion, can be employed in many engineering applications. As was mentioned in Section I, fast-speed streaming motions are highly desired for microfluidics devices. In this regard, the current experimental design can be employed in microfluidics devices. In addition to microfluidics devices, the current experimental apparatus is powerful in the area of boundary layer manipulation and turbulent flow control. The oscillating air-water interface, when duplicated into a closely-compacted array and implemented in a turbulent boundary layer, can effectively modify the structures of the turbulent shear flow and achieve substantial drag reduction effect ($> 40\%$) [22 and 23]. The flow physics discovered in this work provides insights for understanding the physical mechanism of the turbulent drag reduction effect.

The physical mechanism of the current streaming jet is fundamentally different from that of a synthetic jet [24]. A synthetic jet is created by having a piezo-electric actuator oscillating inside a surface cavity, typically in the frequency range of KHz to MHz. The creation of the synthetic jet is due to the actuator periodically adding and subtracting mass flux from the bulk fluid regime through the opening of the surface cavity. As was demonstrated in [25 and 26], the synthetic jet *cannot* be created by only having a flush-mounted piezo-electric actuator without a surface cavity, unless the oscillation magnitude of the actuator is too strong such that cavitation bubbles are generated. In contrast, the presented streaming jet is a special phenomenon that only happens when the oscillation is within certain regimes, without the requirement of addition and subtraction of mass flux through a surface cavity.

The presented streaming jet was not much investigated in the previous studies, which could be due to several reasons. First, it is challenging to theoretically analyze oscillations in the regime with large R and large We. For most of the existing theoretical analysis, a small R (i.e., $R \ll 1$) is generally required so that the analytical streaming function can be expanded into a polynomial of R and the R^2 term is used for analyzing the steady streaming effect [1 and 9]. When R is large, however, either more higher-order terms in the polynomial expansion need to be included in the analysis or a more complicated expansion approach needs to be taken. Oscillations with large R is also less explored by the experimental approach, which could be related to the implementation of the fixed boundary condition and the orientation of the oscillating interface. In many of the previous experimental studies, the cavitation bubble was either freely resting on a flat surface [4] or partially trapped in a surface cavity that has uniform surface wettability 5]. In those scenarios, the contact line of the cavitation bubble is only partially fixed at most. As such, the cavitation bubble may easily detach the solid surface before large amplitude oscillations can be excited. In the current experiment, the enforcement of the fixed contact line boundary condition effectively restricts the mobility of the oscillating cavitation bubble. In addition, the downward orientation of the current interface substantially expands the scope range of the allowed R, because of the stabilization effect of the upward buoyancy force. These unique features of the experiment allow us to investigate well-controlled dynamic oscillations in extended regimes.

The current investigation is limited in several aspects. First, it only considers a small regime in the vast parameter space and categorizes the dynamic oscillations based on R and We only. However, it is possible that many more non-dimensional parameters, such as the Bond number, should be included as well. Second, the effect of the non-dimensional parameter values were only coarsely examined, which cannot provide information for the actual boundary of the streaming pattern change. In addition, the oscillation regimes where other streaming patterns different from the streaming vortex and streaming jet are not explored. In the future, much more extensive parametric studies are needed to comprehensively cover the different streaming patterns and accurately categorize them.

VII. CONCLUSION

In this work we present the dynamic oscillations of an 8 mm diameter axisymmetric air-water interface with a fixed contact line boundary condition. Unlike many of the previous studies, the current investigation explored a regime where the osicillation amplitude is large. Various streaming patterns, such as a ring-shaped vortex or a streaming jet, are induced by the dynamic oscillations. In particular, the streaming jet induced by an oscillating free-slip interface was not reported or studied previously, to the best of the authors' knowledge. The streaming jet is effectively generated when the interface oscillates with a higher-order axisymmetric oscillation modes with a large oscillation amplitude. The streaming jet can be created by an oscillating no-slip elastic membrane as well, when the dynamic oscillation happens in certain regime. From the perspective of vorticity dynamics, the streaming jet is generated and sustained by a process of vorticity generation, transportation, and accumulation happening at the free-slip interface. The streaming jet has many extraordinary characters, such as a high efficacy in generating fast speed streaming motion. These characters make it valuable and useful in a wide range of engineering applications.

ACKNOWLEDGMENTS

This work was supported by the Office of Naval Research under Grant N00014-15-1-2479. Cong Wang was supported by the Stanback Fellowship from the Graduate Aerospace Laboratory of the California Institute of Technology (GALCIT), Caltech.

Appendix A: Material and fabrication procedure of a dynamic no-slip surface

Material: An addition-reaction silicone elastomer (*Elite double 8*, produced by *Zhermack SpA*) is used to fabricate the highly-stretchable elastic membrane. The material can be stretched up to 400% of its original size and has a Youngs modulus of 10^6 N/m^2.

Fabrication procedure: First, the two solutions of *Elite double 8* are well mixed with a ratio of 1 : 1. Second, the mixed solution is poured onto a 6-inch silicon wafer that is spinned by a spin coater at 1000 rpm for one minute. The viscous solution is uniformly spread by the spinning motion to form a thin layer over the flat silicon wafer. Third, the thin layer is settled still for 20 minutes to form an elastic membrane. The measured thickness of the elastic membrane under a microscope is approximately 30 um. The calculated surface tension is 30 N/M, which is about 400 times large of the same sized air-water interface (72 mN/m). Fourth, the membrane is etched using oxygen plasma for 2 minutes so it can form a bond to the *Loctite* super glue. Lastly, the membrane is attached to the flat rim of the surface cavity.

[1] N. Riley, Steady streaming, Annual review of fluid mechanics **33**, 43 (2001).

[2] N. Périnet, P. Gutiérrez, H. Urra, N. Mujica, and L. Gordillo, Streaming patterns in faraday waves, Journal of Fluid Mechanics **819**, 285 (2017).

[3] H. Punzmann, N. Francois, H. Xia, G. Falkovich, and M. Shats, Generation and reversal of surface flows by propagating waves, Nature Physics **10**, 658 (2014).

[4] P. Tho, R. Manasseh, and A. Ooi, Cavitation microstreaming patterns in single and multiple bubble systems, Journal of fluid mechanics **576**, 191 (2007).

[5] C. Wang, B. Rallabandi, and S. Hilgenfeldt, Frequency dependence and frequency control of microbubble streaming flows, Physics of Fluids **25**, 022002 (2013).

[6] T. Luoand M. Wu, Biologically inspired micro-robotic swimmers remotely controlled by ultrasound waves, Lab on a Chip **21**, 4095 (2021).

[7] L. Y. Yeoand J. R. Friend, Ultrafast microfluidics using surface acoustic waves, Biomicrofluidics **3**, 012002 (2009).

[8] B. Rallabandi, C. Wang, and S. Hilgenfeldt, Two-dimensional streaming flows driven by sessile semicylindrical microbubbles, Journal of fluid mechanics **739**, 57 (2014).

[9] M. S. Longuet-Higgins, Viscous streaming from an oscillating spherical bubble, Proceedings of the Royal Society of London. Series A: Mathematical, Physical and Engineering Sciences **454**, 725 (1998).

[10] T. Leighton, *The acoustic bubble* (Academic press, 2012).

[11] J.-H. Kang, Viscously damped free and forced vibrations of circular and annular membranes by a closed form exact method, Thin-Walled Structures **116**, 194 (2017).

[12] S. P. Dasand E. J. Hopfinger, Parametrically forced gravity waves in a circular cylinder and finite-time singularity, Journal of Fluid Mechanics **599**, 205 (2008).

[13] P. K. Farsoiya, Y. Mayya, and R. Dasgupta, Axisymmetric viscous interfacial oscillations–theory and simulations, Journal of Fluid Mechanics **826**, 797 (2017).

[14] S. Basak, P. K. Farsoiya, and R. Dasgupta, Jetting in finite-amplitude, free, capillary-gravity waves, Journal of Fluid Mechanics **909** (2021).

[15] M. Perlinand W. W. Schultz, Capillary effects on surface waves, Annual review of fluid mechanics **32**, 241 (2000).

[16] G. Batchelor, *An introduction to fluid dynamics* (Cambridge university press, 2000).

[17] M. S. Longuet-Higgins, Capillary rollers and bores, Journal of Fluid Mechanics **240**, 659 (1992).

[18] M. Ghariband A. Weigand, Experimental studies of vortex disconnection and connection at a free surface, Journal of Fluid Mechanics **321**, 59 (1996).

[19] G. G. Stokes, On the theory of oscillatory waves, Transactions of the Cambridge philosophical society (1880).

[20] M. S. Longuet-Higgins, Mass transport in water waves, Philosophical Transactions of the Royal Society of London. Series A, Mathematical and Physical Sciences **245**, 535 (1953).

[21] A. Dolev, M. Kaynak, and M. S. Sakar, Dynamics of entrapped microbubbles with multiple openings, Physics of Fluids **34**, 012012 (2022).

[22] C. Wangand M. Gharib, Effect of the dynamic slip boundary condition on the near-wall turbulent boundary layer, Journal of Fluid Mechanics **901** (2020).

[23] C. Wang, D. Jeon, M. Grivel, F. Pereira, and M. Gharib, Systems, methods, and apparatuses for reducing hydrodynamic frictional drag (2020), uS Patent 10,787,231.

[24] A. Glezerand M. Amitay, Synthetic jets, Annual review of fluid mechanics **34**, 503 (2002).

[25] R. James, J. Jacobs, and A. Glezer, A round turbulent jet produced by an oscillating diaphragm, Physics of Fluids **8**, 2484 (1996).

[26] B. L. Smithand A. Glezer, The formation and evolution of synthetic jets, Physics of fluids **10**, 2281 (1998).

[27] P. Marmottantand S. Hilgenfeldt, Controlled vesicle deformation and lysis by single oscillating bubbles, Nature **423**, 153 (2003).

[28] N. Francois, H. Xia, H. Punzmann, and M. Shats, Inverse energy cascade and emergence of large coherent vortices in turbulence driven by faraday waves, Physical review letters **110**, 194501 (2013).

[29] J. Milesand D. Henderson, Parametrically forced surface waves, Annual Review of Fluid Mechanics **22**, 143 (1990).

[30] C. Wangand M. Gharib, Local relaminarization mechanism induced by a dynamic free-slip boundary, Physical Review Fluids **6**, 084604 (2021).